

Interacting Two-Level Systems as a Source of 1/f Noise in Silicon Quantum Dot Qubits

D. L. Mickelsen,¹ Hervé M. Carruzzo,¹ and Clare C. Yu¹

¹*Department of Physics and Astronomy, University of California, Irvine, California 92697, USA*

(Dated: August 29, 2023)

Charge noise in silicon quantum dots has been observed to have a 1/f spectrum. We propose a model in which a pair of quantum dots are coupled to a 2D bath of fluctuating two level systems (TLS) that have electric dipole moments and that interact with each other, i.e., with the other fluctuators. These interactions are primarily via the elastic strain field. We use a 2D nearest-neighbor Ising spin glass to represent these elastic interactions and to simulate the dynamics of the bath of electric dipole fluctuators in the presence of a ground plane representing metal gates above the oxide layer containing the fluctuators. The interactions between the TLS cause the energy splitting of individual fluctuators to change with time. We calculate the resulting fluctuations in the electric potential at the two quantum dots that lie below the oxide layer. We find that 1/f electric potential noise spectra at the quantum dots and cross correlation in the noise between the two quantum dots are in qualitative agreement with experiment. Our simulations find that the cross correlations decrease exponentially with increasing quantum dot separation.

I. INTRODUCTION

Electron spins in Si/SiGe quantum dots (QDs) show promise as quantum bits, but are plagued by charge noise that goes as $1/f^\alpha$ over more than thirteen decades in frequency [1, 2], where f is the frequency and α is the noise exponent. 1/f noise is typically attributed to a bath of two-level fluctuators with a broad distribution of switching rates. If each fluctuator is associated with a double well potential, then thermal activation over a uniform distribution of barrier heights produces 1/f noise [3, 4]. With such a bath of two level systems (TLS), one would expect the charge noise to increase linearly with increasing temperature [5]. However, the measured temperature dependence increasingly deviates from linearity with increasing thickness of the gate oxide layer [6, 7] and, in another study, was found to be quadratic [8].

The small size of the quantum dot and the lack of temperature dependence between 0.45 K and 1.2 K in the decoherence time T_2^* [5] have led some to argue that each quantum dot is only coupled to a few fluctuators [5, 9–11]. This view was supported by the lack of correlation in the charge noise of neighboring quantum dots [6, 7], though subsequent measurements on spin qubit quantum dots have found correlations between the charge noise in neighboring quantum dots that are about 100 nm apart [12] and next-nearest neighbor quantum dots that are about 200 nm apart [13]. With only a few two-level fluctuators, a Lorentzian power spectra is expected instead of the observed 1/f noise.

A number of theoretical papers have considered the effect on silicon qubits of some fluctuators that produce charge noise without going into the detailed microscopics of the fluctuators [14–21], though one group used the measured charge noise spectra to deduce the range of fluctuator rates [22]. Those models that did consider specific types of fluctuators, e.g., charge fluctuator [13], electrons hopping and fluctuators coupled to phonons [23],

had independent, noninteracting fluctuators.

It has been suggested that a few two-level fluctuators can produce 1/f noise if they are coupled to a microscopic subsection of the larger thermal bath [9, 10]. Temperature fluctuations in a subsection of the 2D electron gas (2DEG) are proposed to cause 1/f noise over several decades of frequency, but this model requires that the temperature fluctuations be extremely slow, i.e., the sub-bath would need to remain at a single temperature for unphysically long periods of time in order to explain the low frequency noise [11].

In this paper, we propose that the charge noise arises from a bath of TLS with fluctuating electric dipole moments that reside outside the 2DEG, e.g., in the oxide layer [24]. These TLS interact with one another via elastic and electric dipole moments, though the elastic interactions dominate. (Elastic dipole-dipole interactions are about an order of magnitude larger than electric dipole-dipole interactions [25].) The TLS energy level splittings change with time due to interactions with their fluctuating TLS neighbors. This bath of fluctuating electric dipole moments, together with their image charges in the ground plane lying below the metal gates, produces 1/f noise in the electric potential seen by the quantum dots (QDs) consistent with the observed 1/f charge noise [2]. We find that the correlation of the noise on the quantum dots decreases exponentially with increasing separation between the QDs. When the QDs are about 100 nm apart, the noise is mildly correlated in agreement with experiment [12]. The question of whether the noise in quantum dots is correlated is important because error correcting codes assume that the errors in qubits is independent and uncorrelated [26].

In the next section we describe our model of two quantum dots in a quantum well located below an oxide layer containing a 2D bath of TLS that have both elastic and electric dipole moments. A Monte Carlo simulation of a 2D nearest-neighbor Ising spin glass is used to represent the TLS interacting via the elastic strain field. When

an Ising spin flips, this represents a flip of the elastic dipole moment and the associated electric dipole moment follows along by also flipping. The metallic gates that cover the surface of the device are treated as a ground plane with image charges corresponding to the images of the TLS electric dipole moments. The fluctuating dipole moments and their images produce a fluctuating electric potential at the quantum dots that results in $1/f$ charge noise. We go on to calculate the correlations in the noise at the two quantum dots. These results are presented in section III and discussed in section IV.

II. MODEL

In this section we describe our model that reflects the experimental setup of a pair of quantum dots that are a distance d apart in a quantum well coupled to a bath of TLS with both elastic and electric dipole moments residing in the oxide layer about 30 nm above the quantum well. A set of metal gates lies on top of the oxide layer and are represented by a metal ground plane. The TLS electric dipole moments have image charges in the ground plane; both the electric dipole moments and the image charges contribute to the fluctuating electric potential at the quantum dots. The quantum dots are passive, i.e., they have no internal dynamics; we merely use them to mark the locations where we want to record the charge noise. To determine the dependence of the correlation of the noise on the separation d between the QD, we set $d = 30, 50, 70$ and 100 nm.

Two level systems have long been used to describe the thermal and acoustic properties of amorphous materials at low temperatures [27, 28]. The standard TLS model postulates the existence of independent entities that tunnel between the two minima of a double well potential with a flat distribution of tunnel barrier heights and energy asymmetries [29, 30]. Using a right-well left-well basis, the Hamiltonian representing a given TLS is

$$H_{\text{TLS}} = \frac{1}{2} (\Delta\sigma_z + \Delta_o\sigma_x), \quad (1)$$

where σ_x and σ_z are Pauli matrices, Δ is the TLS asymmetry energy, i.e., the energy difference between the right and left wells, and Δ_o is the tunneling matrix element. The values of these parameters are assumed to vary from TLS to TLS according to the probability distribution:

$$P(\Delta, \Delta_o) = \frac{\bar{P}}{\Delta_o} \quad (2)$$

with $0 < \Delta < \Delta_{\text{max}}$ and $\Delta_{o,\text{min}} < \Delta_o < \Delta_{o,\text{max}}$. \bar{P} is the constant density of states of tunneling entities. The energy eigenvalues of a given TLS are

$$\pm \frac{1}{2} E = \pm \frac{1}{2} \sqrt{\Delta^2 + \Delta_o^2}. \quad (3)$$

Thus the energy splitting between the two levels is E .

TLS interact with electric and elastic fields. A simplified Hamiltonian describing the interactions of a TLS with these fields is given by

$$H_{\text{int}} = \vec{p} \cdot \vec{E}\sigma_z + \gamma\epsilon s\sigma_z, \quad (4)$$

where \vec{p} is the electric dipole moment of the TLS, \vec{E} is the electric field, s represents the random orientation of the elastic dipole, and γ is the magnitude of the interaction between the TLS and the scalar elastic strain field ϵ .

Experimental and theoretical work indicate that TLS interact with each other via the elastic strain field [31–33]. If the TLS have electric dipole moments, then they can also interact via electric fields. However, for reasonable values of the electric dipole moments, the electric dipole-dipole interaction is about an order of magnitude smaller than the elastic dipole-dipole interactions [25]. For example, for $(\text{KBr})_{1-x}(\text{KCN})_x$, the elastic coupling between two CN^- ions is approximately $8 \times 10^3 \text{ K } \text{\AA}^3$ compared to $p^2 \sim 7 \times 10^2 \text{ K } \text{\AA}^3$, where the CN^- dipole moment is $p \sim 0.3 \text{ D}$ [25]. (By coupling, we are referring to the prefactor for the $1/r^3$ dipole term in the Hamiltonian.)

By integrating out the strain field, one can write the interacting Hamiltonian as [34, 35]:

$$H = \frac{1}{2} \sum_{i \neq j} \sigma_i^z \Lambda_{ij} \sigma_j^z. \quad (5)$$

Here Λ_{ij} is given (in simplified form) by:

$$\Lambda_{ij} = \left(\frac{\gamma^2}{\rho v^2} \right) \frac{s_i s_j}{r_{ij}^3}, \quad (6)$$

where ρ is the density of the material, v is the speed of sound, and r_{ij} is the distance between TLS i and j . We make the simplification that the orientation of the elastic dipole is binary, i.e., $s_i = \pm 1$ is an Ising spin representation of the orientation of the elastic dipoles (see [34] for the full expressions). We can rewrite the Hamiltonian in terms of local fields produced by the neighboring TLS:

$$H = \frac{1}{2} \sum_i h_i \sigma_i^z, \quad (7)$$

where

$$h_i = \sum_{j \neq i} \Lambda_{ij} \sigma_j^z. \quad (8)$$

Fluctuations in the neighboring TLS, i.e., flips in s_j , produce fluctuations the local field and hence in the energy splitting of the i th TLS. This leads to relaxation times that vary in time since the TLS relaxation rate is given by [27, 28]:

$$\tau^{-1} = \frac{\gamma^2}{\rho} \left[\frac{3}{v^5} \right] \frac{E^3}{2\pi\hbar^4} \left[\frac{\Delta_o}{E} \right]^2 \coth \left(\frac{\beta E}{2} \right), \quad (9)$$

where $\beta = 1/k_B T$ is the inverse temperature. As a result, a large number of fluctuators with a broad distribution of relaxation times can produce $1/f$ noise [36–38]. However, a quantum dot will not be equally affected by a large number of fluctuators. Rather, the TLS nearest to the QD will have the greatest influence on its charge noise spectrum. So we will explore a different mechanism to explain $1/f$ charge noise.

Furthermore, it is the electric dipole moments, not the elastic dipole moments, that couple to quantum dots and give rise to charge noise. We assume that when a TLS tunnels from one well to the other, both its elastic and electric dipole moments flip. This results in fluctuations in the electric potential $V(t)$ seen by the QDs. Since there is a metal ground plane, both the electric dipole moments \vec{p} and their image charges will contribute to $V(t)$ which is given by

$$V_\zeta(t) = \sum_{\eta=1}^2 \sum_{i=1}^N \frac{\vec{p}_{\eta,i}(t) \cdot \hat{R}_{\eta,i,\zeta}}{R_{\eta,i,\zeta}^2}, \quad (10)$$

where $\zeta = 1, 2$ denotes the QD, the sum over i corresponds to summing over TLS in the oxide layer (denoted by $\eta = 1$) and their images (denoted by $\eta = 2$). $R_{\eta,i,\zeta}$ is the distance between the electric dipole $\vec{p}_{\eta,i}$ and the ζ th quantum dot, and $\hat{R}_{\eta,i,\zeta}$ is a unit vector that points from the dipole to the ζ th quantum dot.

We represent the TLS electric dipoles by a 2D square lattice of dipoles that are randomly oriented. We set the magnitudes of each dipole moment to unity. The mirror images of these electric dipoles in the ground plane form a second 2D square lattice. The dynamics of the TLS is governed by their elastic interactions which we model very simply with a 2D nearest neighbor Ising spin glass on a square lattice. Each Ising spin represents a TLS elastic dipole. When the Ising spin (elastic dipole) flips, its corresponding electric dipole moment, as well as its image electric dipole moment, flips 180° . In some sense the Ising spin is an avatar or proxy for the electric dipole moment. Flips of electric dipoles and their images will change the electric potential $V_i(t)$ seen by the i th quantum dot and given by Eq. (10). The time series of $V_i(t)$ is Fourier transformed to produce the charge noise power spectrum.

For the purposes of our simulation, it does not matter whether the transitions between the two states of a TLS occur via tunneling or thermal activation because we assume there is no coherence between successive transitions. Thus we represent a TLS elastic dipole by an Ising spin. Since TLS occur at random locations, their interactions are random. So we will use a nearest-neighbor Ising spin glass to model the interacting TLS bath.

A. Simulation Details

We performed Monte Carlo simulations of a 2D Ising spin glass on a square 16×16 lattice with periodic

boundary conditions. Each Ising spin corresponds to a TLS with an elastic dipole moment. The Hamiltonian is given by

$$H = - \sum_{\langle i,j \rangle} J_{ij} S_i S_j, \quad (11)$$

where S_i and S_j are Ising spins with values ± 1 on nearest neighbor sites i and j , respectively. J_{ij} is the nearest neighbor coupling. It represents the elastic coupling between TLS. We use a spin glass distribution of couplings chosen from a normal distribution centered at $J_{ij} = 0$ with a variance $\sigma_{J_{ij}}^2 = 1$. A positive value for J_{ij} indicates a ferromagnetic interaction.

We can rewrite the Hamiltonian in terms of local fields h_i :

$$H = - \frac{1}{2} \sum_i h_i S_i, \quad (12)$$

where the local field of S_i is produced by the neighboring spins:

$$h_i = \sum_j J_{ij} S_j. \quad (13)$$

The Ising spins are initialized at infinite temperature with randomly oriented spins. A spin is allowed to reorient itself according to the Metropolis algorithm [39]. In this algorithm, a trial move consists of first choosing a spin on the lattice at random. For a given temperature T , the initial energy $E_i = h_i S_i$ of this site is calculated using Eq. (13) from the local field produced by its nearest neighbors. The orientation of the spin is reversed in a trial move, and the final energy E_f of this site with the new spin orientation is calculated. If the final energy is less than the initial energy, then the spin flip is accepted. However, if the final energy is greater than the initial energy, then the Boltzmann factor $\exp[-(E_f - E_i)/(k_B T)]$ is calculated. If a random number generated from a uniform distribution between 0 and 1 is less than this Boltzmann factor, then the new orientation is accepted. This process continues for the remaining sites within the lattice until all the spins in the lattice have been given an opportunity to flip. The time it takes for one sweep through the lattice is one Monte Carlo step (MCS).

The Ising spin glass is cooled from its initial infinite temperature spin configuration at $T = 10$ to $T = 0.6$. At each temperature, after an initial equilibration time of 10^5 MCS, we check to see if the system is equilibrated using the method of Bhatt and Young [40]. Details of the equilibration are given in Appendix A.

Each TLS has an electric dipole moment. These electric dipoles are initialized with random orientations. Since the electric dipole-dipole interaction is an order of magnitude smaller than the elastic dipole-dipole interaction, it is the elastic interactions between TLS that governs their dynamics. We represent these dynamics by the Ising spin glass described above. Thus, each electric

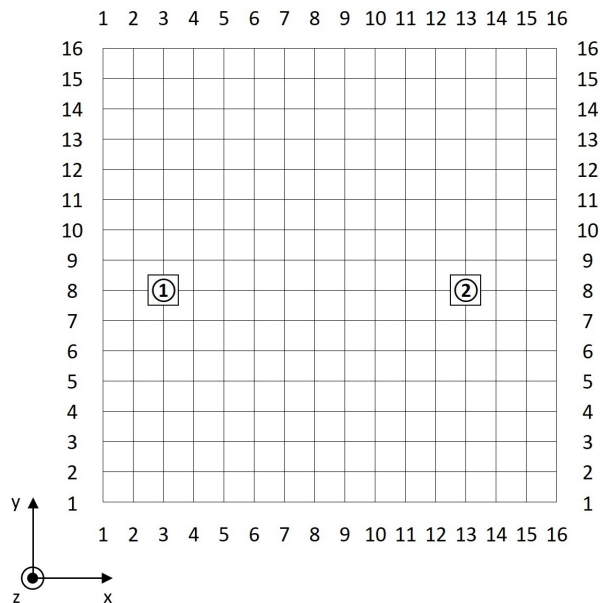


FIG. 1. 16×16 lattice with an electric dipole occupying every site. The circled 1 and 2 represent quantum dots that are 10 lattice spacings apart in a plane that is three lattice spacings beneath the main lattice.

dipole has a corresponding Ising spin. If the Ising spin flips, then the corresponding electric dipole and its image dipole flip 180° . We consider two cases of electric dipole orientations. In both cases, the magnitude of the dipole moment is unity. In the first case, the dipoles are randomly oriented with random x, y, and z components. To better understand the contribution of each component, we also consider a second case where the dipole all lie parallel to one another along the x, y, or z axis, though they are randomly oriented in the positive or negative direction.

Let us take a moment to describe the device geometry that we have in mind. TLS that have both an electric and an elastic dipole moment are located on every site of a 16×16 square lattice. We envision these TLS to reside in the oxide layer of a Si/Si-Ge heterostructure with a quantum well. Since TLS are typically about 10 nm apart, we take the lattice spacing to be 10 nm; this sets the length scale. A second 16×16 square lattice is located half a lattice spacing above the first lattice and is populated by the image dipoles that result from the ground plane formed by metal gates. We consider two QDs about 100 nm apart located in a quantum well about 30-50 nm below the oxide layer. So in our simulation two QDs plane are separated by 10 lattice spacings in a plane located 3 lattice spacings below the first electric dipole lattice. This is illustrated in Figure 1. To see how the correlations of the charge noise depend on the distance between QDs, we also considered cases where the QDs were separated by 3, 5, and 7 lattice spacings in the plane representing the oxide layer.

B. Noise Power, Exponents, and Correlation Functions

The fluctuating electric dipole moments produce a time dependent electric potential $V_i(t)$ at the i th QD given by Eq. (10). After equilibration of the Ising spin glass, the potential is recorded at every Monte Carlo step, resulting in a time series that can be Fourier transformed to obtain the charge noise power spectrum. The deviation from the average is $\delta V_i(t) = V_i(t) - \overline{V_i(t)}$. The noise power spectral density can be determined from the Fourier transform of the autocorrelation function $C_i(\tau) = \int_{-\infty}^{\infty} \delta V_i(t) \delta V_i(t + \tau) dt$. For a time series of length t_{total} : $S(f) = \frac{1}{t_{\text{total}}} \int_{-\infty}^{\infty} C_i(\tau) e^{-2\pi i f \tau} d\tau$. A useful method for computing the power spectrum is the periodogram estimate [41]:

$$S_i(f) = \frac{1}{t_{\text{total}}} |\delta V_i(f)|^2, \quad (14)$$

where t_{total} is the length of the potential time series, and $\delta V(f)$ is the Fourier transform of the electric potential time series. The Fourier transform is computed using the C subroutine library FFTW [42]. At a given temperature, the time series $V_i(t)$ is split into ten segments of equal length. The power spectrum is found for each segment and is averaged over these segments to give a smoother power spectrum. The power spectrum is normalized so that

$$P_{i,\text{total}} = \frac{2}{t_{\text{total}}} \sum_{f=0}^{f_{\text{max}}} S_i(f) = \sigma_{V_i}^2, \quad (15)$$

where P_{total} is the total noise power and $\sigma_{V_i}^2$ is the variance in the electric potential of the i th QD. To determine the noise exponent α , the function A^2/f^α is fit to power spectra (averaged over 10 segments) in the vicinity of a fixed frequency because experiments typically determine noise exponents at 1 Hz.

To calculate the correlation between the fluctuating dipole potentials $V_1(t)$ and $V_2(t)$, we use the Pearson correlation coefficient that is given by:

$$\rho_{V_1(t), V_2(t)} = \frac{\langle \delta V_1(t) \delta V_2(t) \rangle_t}{\sigma_{V_1(t)} \sigma_{V_2(t)}}, \quad (16)$$

where $\delta V_1(t)$ and $\delta V_2(t)$ are the fluctuations in the potentials about their average. $\sigma_{V_1(t)}$ and $\sigma_{V_2(t)}$ are the standard deviations of the potentials. To calculate the correlations, the time series $V_1(t)$ and $V_2(t)$ are divided into ten blocks of equal size. The correlation is calculated for each of the ten blocks using Eq. (16), and the standard deviation is calculated from the ten correlations. The correlations and standard deviations are then averaged over 200 independent runs.

We also calculate the noise correlation between the two QDs as a function of frequency as was done in [12]. We

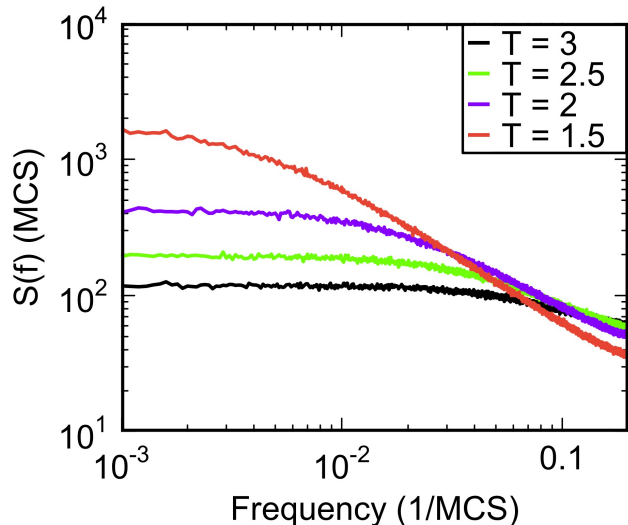


FIG. 2. Plots of the electric dipole potential noise power at QD 1 vs. frequency for $1.5 \leq T \leq 3$ averaged over 200 runs. The noise is produced by fluctuating electric dipoles with random orientations. The QDs are 10 lattice spacings apart.

use:

$$\rho_{V_1(t), V_2(t)}(f) = \frac{\langle \delta \tilde{V}_1(f) \delta \tilde{V}_2^*(f) \rangle_{\text{blocks, runs}}}{\sqrt{\langle S_{V_1}(f) \rangle_{\text{blocks, runs}} \langle S_{V_2}(f) \rangle_{\text{blocks, runs}}}}, \quad (17)$$

where $\delta \tilde{V}_1(f)$ and $\delta \tilde{V}_2(f)$ are the Fourier transforms of the fluctuations in the potentials about their average. $S_{V_1}(f)$ and $S_{V_2}(f)$ are the noise power of the dipole potentials at quantum dots 1 and 2. To calculate the numerator of Eq. (17), the time series $V_1(t)$ and $V_2(t)$ are divided into 100 blocks of equal size. For each block, the Fourier transforms of the fluctuations are calculated. The product $\delta \tilde{V}_1(f) \delta \tilde{V}_2^*(f)$ is averaged over the 100 blocks and 200 runs to give $\langle \delta \tilde{V}_1(f) \delta \tilde{V}_2^*(f) \rangle_{\text{blocks, runs}}$. To calculate the denominator of Eq. (17), the power spectra $S_1(f)$ and $S_2(f)$ are calculated for each block. Then $S_1(f)$ and $S_2(f)$ are each averaged over the 100 blocks and 200 runs to give $\langle S_{V_1}(f) \rangle_{\text{blocks, runs}}$ and $\langle S_{V_2}(f) \rangle_{\text{blocks, runs}}$. The denominator of the correlation is then calculated and used in Eq. (17). Since the frequency-dependent correlation function in Eq. (17) is a complex number, we plot its magnitude and phase as a function of frequency.

III. RESULTS

Figure 2 shows the noise power at QD 1 at various temperatures for randomly oriented dipoles averaged over 200 runs. To determine the amplitude $A^2(T)$ and the noise exponent $\alpha(T)$, the function $A^2(T)/f^{\alpha(T)}$ is fit to the region of the power spectra that is linear on a log-log

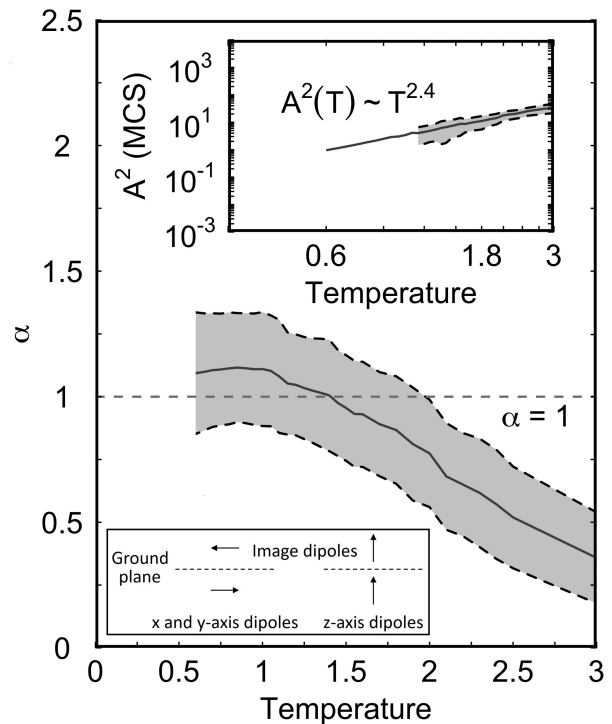


FIG. 3. Plot of the temperature dependence of the noise exponent, $\alpha(T)$, of the electric potential noise power spectra at QD 1 resulting from fluctuating electric dipoles with random orientations for $0.6 \leq T \leq 3$. The solid line in the middle is the average noise exponent over 200 runs. The top and bottom dashed lines are one standard deviation above and below the mean. Upper inset: Log-log plot of the temperature dependence of the electric potential noise power amplitude, $A^2(T)$, at QD 1 resulting from fluctuating electric dipoles with random orientations for $0.6 \leq T \leq 3$. The central solid line is the amplitude averaged over 200 runs. The top and bottom dashed lines of the shaded region are one standard deviation above and below the mean amplitude. The lack of shading at low temperatures is due to the standard deviation being greater than the mean which cannot be shown on a logarithmic scale. The QDs are 10 lattice spacings apart in the main plot and in the upper inset. Lower inset: Orientation of dipoles and their dipole images.

plot. The noise exponent $\alpha(T)$ as a function of temperature is shown in Fig. 3. Experimentally, in the temperature range from 50 mK to 1 K, the noise exponents within one standard deviation of the mean at 1 Hz ranged from about 0.65 to 1.3 [6, 43]. In our simulations the noise exponents increase from zero at high temperatures to approximately 1.15 at low temperatures which is roughly consistent with experiment.

The noise amplitude $A^2(T)$ shown in the inset of Fig. 3 goes as $T^{2.4}$. For an ensemble of fluctuators with thermally activated switching rates and a flat distribution of activation energies, one would expect the noise amplitude to increase linearly with temperature [5]. However, as we mentioned in the introduction, experiments find

the temperature dependence of the noise at 1 Hz increasingly deviates from linearity with increasing thickness of the gate oxide layer [6, 7] and, in another study, was found to be quadratic [8]. So our simulation results are qualitatively consistent with experiment but the reason why is not clear. We will consider this further in the discussion section.

If one considers the contributions of the different components of the dipoles to the charge noise, one realizes that the z-component dominates because the z-component of the image dipole in the ground plane (that lies perpendicular to the z-axis) points in the same direction as the z-component of the original dipole (see lower inset in Figure 3). However, the x and y components of the image dipole point in the opposite direction of the x and y components, respectively, of the original dipole (see lower inset in Figure 3). To confirm this, we have performed simulations for dipoles that lie along either the x, y, or z axis (see Appendix B for details of the simulations). The results are shown in Figures 10 and 11 in Appendix B. One can see that the noise produced by the dipoles along the z-axis is about two orders of magnitude larger than that associated with dipoles along the x or y axes. Comparing the plots in Fig. 10 with the corresponding plots (Figs. 2, 3, and 4) for randomly oriented dipoles, we see the marked similarity between the results for the dipoles along the z-axis and the randomly oriented dipoles. However, the noise power and noise amplitudes resulting from electric dipoles aligned along the z-axis are three times larger than that of the randomly oriented dipoles because the z-axis dipoles have unit length, while the z components of the randomly-oriented dipoles have a typical length of $1/\sqrt{3}$.

Using Eq. (16), we calculated the correlation in the noise for various separations between QD 1 and QD 2 as shown in Fig. 4. The correlation decreases exponentially with increasing distance between the QDs. At a separation of 10 lattice spacings corresponding to about 100 nm, we can see from Fig. 4 that there is some correlation between QDs 1 and 2 which is consistent with experiment. As we mentioned earlier, recent measurements find that there are correlations in the charge noise between quantum dots that are about 100 nm apart [12] and 200 nm apart [13]. Furthermore, Ref. [13] found that charge noise correlations decayed exponentially up to a few hundred nm and then decayed as a power law $\sim d^{-a}$ where d is the QD separation and the exponent a varied between 4 and 5.

We used Eq. (17) to calculate the frequency dependence of the magnitude and phase of correlations in the noise produced by randomly oriented fluctuating electric dipoles. These results are shown in Figure 5 for QDs separated by distances of 3, 5, 7, and 10 lattice spacings.

To better understand these correlations in the noise, we considered the more realistic case of two QDs separated by 10 lattice spacings. We used Eq. (17) to calculate the frequency dependence of the magnitude and phase produced by randomly oriented fluctuating elec-

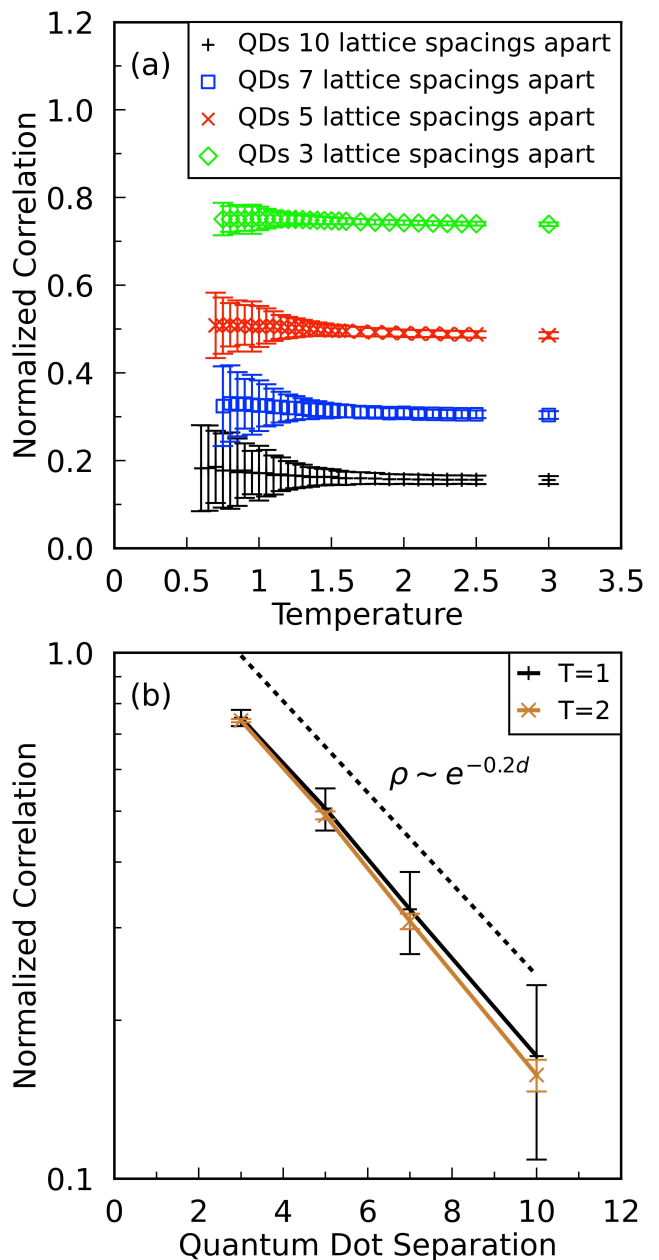


FIG. 4. (a) Plot of electric potential noise correlations for between QDs 1 and 2 vs. temperature for $0.8 \leq T \leq 3$ resulting from fluctuating electric dipoles with random orientations. QD separations of 3, 5, 7 and 10 lattice spacings are shown. (b) Lin-log plot of the charge noise correlations between QDs as a function of QD separation at $T = 1$ and $T = 2$. The noise correlations decrease exponentially with increasing QD separation d .

tric dipoles as well as dipoles aligned along various axes (see Figure 6). Fig. 6(a) shows that there is correlation in the noise between the two dots as we saw in the Pearson correlation. These correlations are due largely to the geometry of the location of the dipoles with respect to the QDs. There is no noticeable frequency dependence

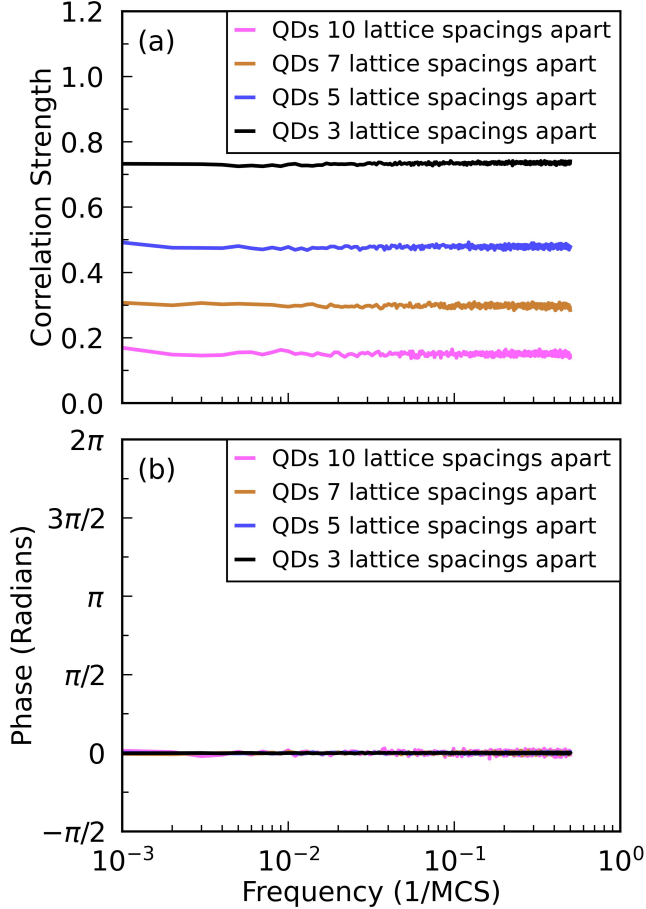


FIG. 5. Plots of the (a) magnitude and (b) phase of electric potential noise correlations between QDs 1 and 2 vs. frequency at $T = 1$ for QD separations of 3, 5, 7 and 10 lattice spacings. The noise correlations decrease with increasing distance. The noise arises from fluctuating electric dipoles with random orientations.

in either the magnitude or the phase of the correlations because unlike the experimental case [12], our QDs have no dynamics.

The magnitude of the noise correlation is larger for the x-axis and z-axis dipoles compared to the y-axis dipoles, and comparable to that for randomly oriented dipoles (see Figs. 10(f) and 6(a)). Even though the numerator of Eq. (17) is about two orders of magnitude larger for dipoles aligned along the z-axis compared to those aligned along the x-axis, the normalization by the noise amplitude in the denominator makes the noise correlation of the x and z axis dipoles comparable. The sizeable contribution of the x-axis dipoles, especially those located at or near the same y-coordinate as the QDs, is due to the large value of $(\vec{p}_{\eta,i}(t) \cdot \hat{R}_{\eta})$, the numerator of Eq. (10), coupled with the small value of the denominator $R_{\eta,i}^2$. $(\vec{p}_{\eta,i}(t) \cdot \hat{R}_{\eta})$ is large when $\vec{p}_{\eta,i}(t)$ is collinear with \hat{R}_{η} . On the other hand, the y-axis dipoles have small values of $(\vec{p}_{\eta,i}(t) \cdot \hat{R}_{\eta})$ when the y-coordinate of their location is

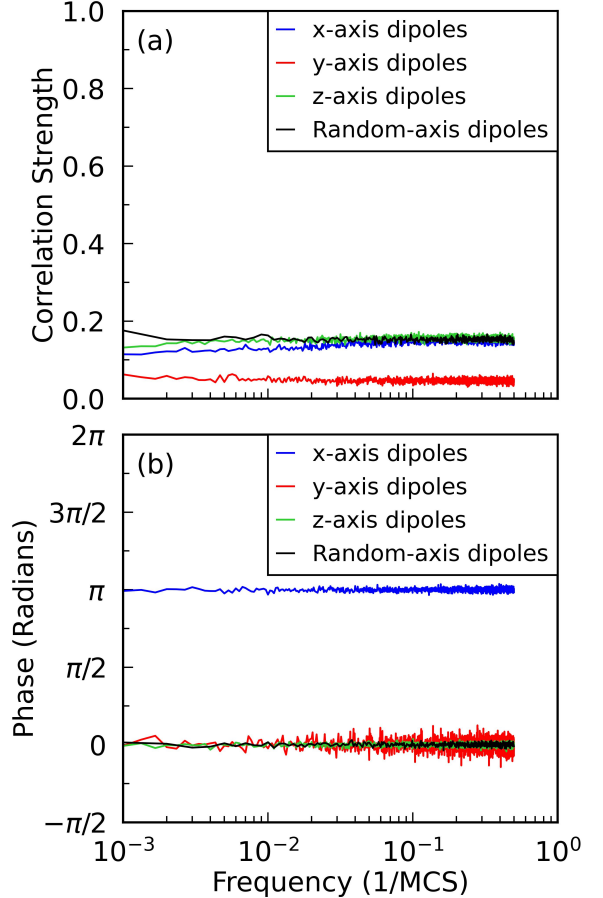


FIG. 6. Plots of the (a) magnitude and (b) phase of electric potential noise correlations between QDs 1 and 2 that are 10 lattice spacings apart as a function of frequency for fluctuating electric dipoles with fixed (x, y, and z) and random orientations at $T = 1$. Plots are the result of averaging over 200 runs.

comparable to that of the QDs because the y-axis dipole is almost perpendicular to the unit vector \hat{R}_{η} pointing from the dipole to the QD. Again z-axis dipoles give large contributions because their image charges lie in the same direction as the z-axis dipoles themselves.

Figure 6(b) shows that the correlations produced by the x-axis dipoles are 180° out of phase. This is due to the fact that since the QDs lie along the x-axis, flips in the x-axis dipoles located between the QDs will have the opposite effect on each dot due to the factor $(\vec{p}_{\eta,i}(t) \cdot \hat{R}_{\eta})$ in the numerator of Eq. (10).

IV. DISCUSSION

We have proposed a model in which the $1/f$ charge noise in quantum dots is due to a bath of electric dipole fluctuators that interact with each other primarily via the elastic strain field. We use a 2D nearest-neighbor Ising spin glass to represent these elastic interactions and to

simulate the dynamics of the bath of electric dipole fluctuators in the presence of a ground plane representing metal gates above the oxide layer containing the fluctuators. We find $1/f$ noise spectra with a temperature dependent amplitude that are in qualitative agreement with experiment. Likewise, the noise correlations between quantum dots are also in qualitative agreement with experiment, with the correlations decreasing exponentially with increasing QD separation.

Unlike previous theoretical models which focused on the effects on qubits of charge noise produced by independent charge fluctuators, we focused on interacting TLS with only placeholders for qubits. Interactions between TLS cause the dynamics and energy splitting of individual TLS to change with time, leading to noise spectra that have a range of noise exponents as has been observed experimentally.

We found that the noise amplitude $A^2(T)$ goes as $T^{2.4}$ as shown in the inset of Fig. 3 which is consistent with experiment [6–8]. This implies a nonuniform distribution of barrier heights [6, 7]. We cannot deduce the distribution of barrier heights from our simulations. Ising spins do not have activation barriers per se; they simply flip based on the energy difference between the initial and final states. The distribution of local fields $P(h)$ is analogous to the distribution of TLS asymmetry energies, but it does not capture the barrier heights of the energy landscape. In our simulations, the low frequency behavior of charge noise involves multiple spin flips and dynamics that explore the TLS energy landscape at long time scales.

As we mentioned earlier, the other mechanism by which TLS produce slow fluctuations is via tunneling through a barrier, leading to long relaxation times as given in Eq. (9). A broad distribution of relaxation rates associated with noninteracting tunneling TLS produces $1/f$ charge noise that increases linearly with temperature, i.e., $S(f) \sim T/f$ [36–38]. However, a quantum dot is not equally coupled to a large number of fluctuators, i.e., it does not equally weight the broad distribution of relaxation times. Rather, the TLS (and their images) closest to a QD have the greatest influence on its charge noise. The more distant TLS affect the QD less, though the number of these distant TLS grows as the square of the distance, assuming a constant density in the 2D oxide layer. Furthermore, as we mentioned in the introduction, the experimentally measured temperature dependence increasingly deviates from linearity with increasing thickness of the gate oxide layer [6, 7] and, in another study, was found to be quadratic [8]. In our simulations, the interactions between the TLS cause their energy splittings and flipping rates to change, leading to $1/f$ noise with an amplitude that increases as $A^2 \sim T^{2.4}$, consistent with experiment.

In summary, our work highlights the importance of two level fluctuators and their mutual interactions in producing $1/f$ charge noise in silicon qubits.

ACKNOWLEDGMENTS

We thank Sue Coppersmith for bringing this problem to our attention and for helpful discussions. This work was performed in part at the Aspen Center for Physics, which is supported by National Science Foundation grant PHY-2210452.

Appendix A: Equilibration

1. Equilibration and Recording Times

The Ising spin glass systems are equilibrated for 10^5 MCS at $T = 10$. As the system is cooled, the equilibration and recording times are increased if the system is not in equilibrium. These times as a function of temperature are shown in Table I.

Temperature	Equilibration and Recording Times (MCS)
$1 \leq T \leq 10$	10^5
$0.8 \leq T \leq 0.95$	3×10^5
$T = 0.75$	10^6
$0.65 \leq T \leq 0.7$	3×10^6
$T = 0.6$	10^7

TABLE I. Equilibration and recording times for the 2D (16×16) Ising spin glass with random electric dipole orientations for $0.6 \leq T \leq 10$.

2. Spin Glass Susceptibility

The test for equilibration follows Bhatt and Young’s procedure for the equilibration of Ising spin glasses [40]. Two independent replicas of each system with the same exchange couplings are created and run in parallel. The initial spin configurations for the two replicas are different and random. For the set of spins $\{s_i\}$ with N lattice sites, the spin autocorrelation function for the replica n , after an equilibration time t_0 , is

$$Q^{(n)}(t) = \frac{1}{N} \sum_{i=1}^N s_i^{(n)}(t_0) \cdot s_i^{(n)}(t_0 + t), \quad (\text{A1})$$

where the summation is over all lattice sites. The spin glass susceptibility for replica n is calculated as the second moment of this overlap and then averaged over 200 different realizations of bonds and anisotropy axes. This disorder average is denoted by $[\dots]_{\text{av}}$:

$$\chi_{\text{SG}}^{(n)}(t) = \frac{1}{N} \left[\left(\sum_{i=1}^N s_i^{(n)}(t_0) \cdot s_i^{(n)}(t_0 + t) \right)^2 \right]_{\text{av}}. \quad (\text{A2})$$

The equilibration time t_0 is chosen from the sequence 1, 3, 10, 30, 100, 300, \dots , etc. The idea is to compare

$s_i^{(n)}(t_0)$ to $s_i^{(n)}(t_0+t)$ as $t \rightarrow \infty$ to see whether $s_i^{(n)}(t_0+t)$ has lost its “memory” of $s_i^{(n)}(t_0)$. In practice, the comparison is done as $t \rightarrow t_0$. The spin glass susceptibility in Eq. (A2) is averaged over a length of time t_0 :

$$\chi_{\text{SG}}^{(n)} = \frac{1}{Nt_0} \left[\sum_{t=t_0}^{2t_0-1} \left(\sum_{i=1}^N s_i^{(n)}(t_0) \cdot s_i^{(n)}(t_0+t) \right)^2 \right]_{\text{av}}. \quad (\text{A3})$$

The summation over t starts at t_0 so that the distribution of $Q^n(t)$ is Gaussian. The correlation of the spins at shorter times makes the distribution deviate from a Gaussian.

For small values of t_0 and when the system is at low temperatures, there are few spin fluctuations, so $Q^{(n)}(t) \sim 1$ and $\chi_{\text{SG}}^{(n)}(t) \sim N$. This is in agreement with simulations.

We can also calculate $\chi_{\text{SG}}^{(n)}$ in the high-temperature limit. We start with two Ising spins s_1 and s_2 that represent $s_i^{(n)}(t_0)$ and $s_i^{(n)}(t_0+t)$, respectively, in Eq. (A3). The average square of the dot product is calculated as

$$\begin{aligned} \langle (s_1 \cdot s_2)^2 \rangle_{\text{Ising}} &= \langle (\pm s_1 s_2)^2 \rangle \\ &= \langle s_1^2 s_2^2 \rangle \\ &= 1. \end{aligned} \quad (\text{A4})$$

Combining Eq. (A4) with Eq. (A3), for high temperatures, we get $\chi_{\text{SG}}^{(n)} = 1$ which is seen in simulations.

We then define the average of the two single replica susceptibilities

$$\bar{\chi}_{\text{SG}} = \frac{1}{2} \left(\chi_{\text{SG}}^{(1)} + \chi_{\text{SG}}^{(2)} \right) \quad (\text{A5})$$

as the two times spin glass susceptibility.

The spin glass susceptibility may also be calculated from the spin overlap of the two different replicas. The mutual overlap between the spins $s_i^{(1)}$ and $s_i^{(2)}$ of the two replicas is

$$Q(t) = \frac{1}{N} \sum_{i=1}^N s_i^{(1)}(t_0+t) \cdot s_i^{(2)}(t_0+t). \quad (\text{A6})$$

The spin glass susceptibility is calculated from the spin overlap:

$$\chi_{\text{SG}} = \frac{1}{Nt_0} \left[\sum_{t=t_0}^{2t_0-1} \left(\sum_{i=1}^N s_i^{(1)}(t_0+t) \cdot s_i^{(2)}(t_0+t) \right)^2 \right]_{\text{av}}. \quad (\text{A7})$$

For all temperatures, as the equilibration time is approached, the spin glass susceptibilities converge; the two times susceptibility $\bar{\chi}_{\text{SG}}$ (Eq. (A5)) approaches the true susceptibility from above and the replica susceptibility χ_{SG} (Eq. (A7)) from below. This is shown in Fig. 7 for the Ising spin glass at $T = 2$.

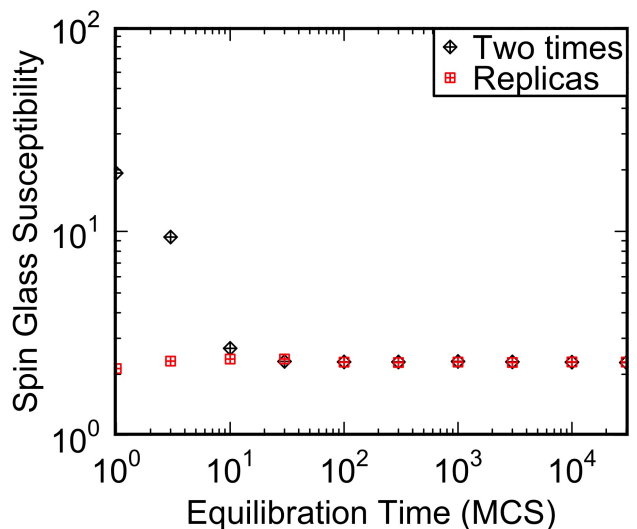


FIG. 7. Two times and replica susceptibility for the 2D (16×16) Ising spin glass for $T = 2$ averaged over 200 runs. For sufficiently long equilibration times, the two susceptibilities agree, and the system is in equilibrium.

After sufficiently long equilibration times, χ_{SG} and $\bar{\chi}_{\text{SG}}$ agree. We define the system to be equilibrated if

$$\Delta\chi_{\text{SG}} = \frac{|\chi_{\text{SG}} - \bar{\chi}_{\text{SG}}|}{\frac{1}{2}(\chi_{\text{SG}} + \bar{\chi}_{\text{SG}})} \quad (\text{A8})$$

is less than 5% for three consecutive times in the t_0 sequence; then we declare it equilibrated at the fourth time. For example, if the last three equilibration times are $t_1 = 3 \times 10^3$, $t_2 = 10^4$, $t_3 = 3 \times 10^4$, then the equilibration time $t_4 = 10^5$. At each temperature, the initial equilibration time is 10^5 MCS, and it is increased if the system is not equilibrated.

3. Specific Heat and Susceptibility

As a check of this equilibration method, we calculate the block-averaged specific heat and magnetic susceptibility in a similar method to Yu and Carruzzo [44]. We use the form of specific heat

$$\begin{aligned} C_V &= \frac{1}{k_B T^2} (\langle E^2 \rangle - \langle E \rangle^2) \\ &= \frac{N_{\text{sites}}^2}{k_B T^2} (\langle e^2 \rangle - \langle e \rangle^2), \end{aligned} \quad (\text{A9})$$

where $k_B = 1$, T is temperature, E is the total energy of the lattice, N_{sites} is the total number of sites, and e is the total energy of the lattice divided by the number of sites. In a similar form, we have the magnetic susceptibility

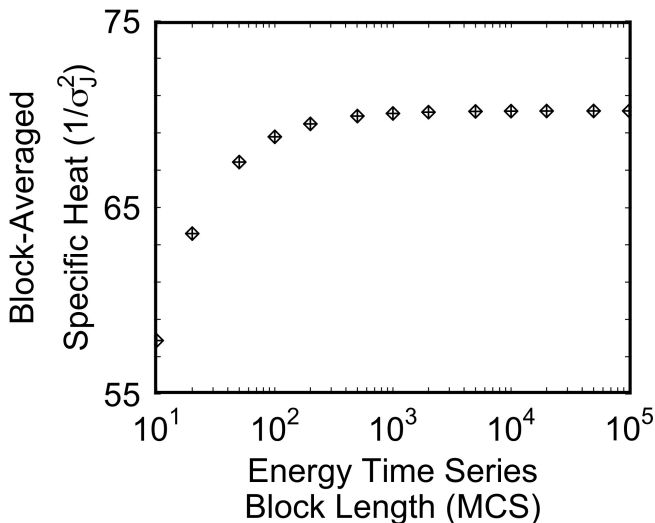


FIG. 8. Block-averaged specific heat versus energy time series block length for the 2D (16×16) Ising spin glass at $T = 2$ averaged over 200 runs. For longer time series, the specific heat approaches a constant value.

$$\begin{aligned} \chi &= \frac{1}{k_B T} (\langle M^2 \rangle - \langle M \rangle^2) \\ &= \frac{N_{\text{sites}}^2}{k_B T} (\langle m^2 \rangle - \langle m \rangle^2), \end{aligned} \quad (\text{A10})$$

where $k_B = 1$, T is temperature, M is the total magnetization of the lattice, N_{sites} is the total number of sites, and m is the total magnetization of the lattice divided by the number of sites.

To calculate the block-averaged specific heat, the energy time series of the system is divided into equally-sized blocks. The specific heat is calculated for each block using Eq. (A9), and then the blocks are averaged together. For larger block sizes, the specific heat increases and eventually levels off. The block-averaged specific heat is shown in Fig. 8. The temperature is in units of the standard deviation of the exchange couplings. In our simulations of the Ising spin glass, $\sigma_J = 1$.

To calculate the block-averaged magnetic susceptibility, we follow a similar procedure, but we use Eq. (A10) with the magnetization time series. The block-averaged magnetic susceptibility is shown in Fig. 9.

We can see qualitatively that the results of Figs. 8 and 9 are consistent with the spin glass equilibration results of Fig. 7. They indicate that the system is in equilibrium after $\approx 10^3$ MCS.

Appendix B: Dipoles aligned along the x, y, or z axes

We perform another 200-run set of Monte Carlo simulations of 2D (16×16) Ising spins. In this case, the

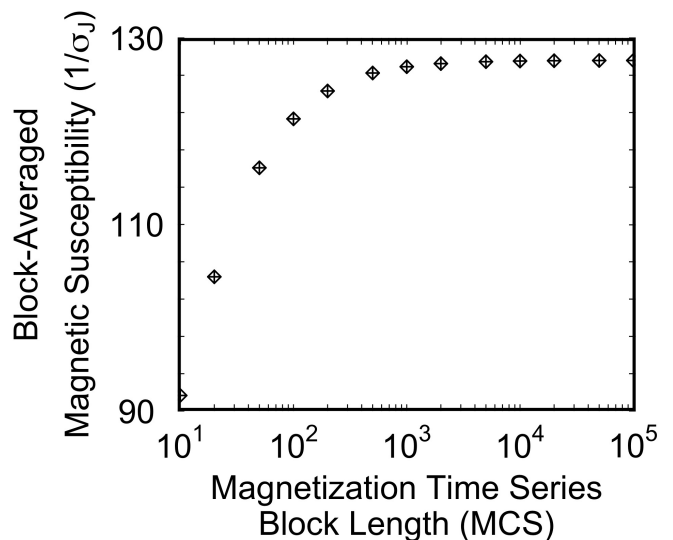


FIG. 9. Block-averaged magnetic susceptibility versus magnetization time series block length for the 2D (16×16) Ising spin glass at $T = 2$ averaged over 200 runs. For longer time series, the magnetic susceptibility approaches a constant value.

electric dipoles lie along the x, y, or z axis. The equilibration times are shown in Table II.

Temperature	Equilibration and Recording Times (MCS)
$1.05 \leq T \leq 10$	10^5
$0.85 \leq T \leq 1$	3×10^5
$0.7 \leq T \leq 0.8$	10^6
$0.6 \leq T \leq 0.65$	10^7

TABLE II. Equilibration and recording times for the 2D (16×16) Ising spin glass with dipoles that lie along the x, y, or z axis for $0.6 \leq T \leq 10$.

The noise power as a function of frequency are shown in Fig. 10 for electric dipoles aligned along the (a) x-axis, (b) y-axis, and (c) z-axis.

$A^2(T)/f^{\alpha(T)}$ is fit to the region of the power spectra that is linear on a log-log plot. The noise amplitudes ($A^2(T)$) and exponents ($\alpha(T)$) are shown in Fig. 11 (a) and (b), respectively. The dipole correlations are calculated for each axis using Eq. (16), and they are shown in Fig. 11 (c).

The frequency-dependent correlation and phase for the fixed-axis dipoles are calculated using Eq. (17). The correlation and phase are shown in Fig. 6. For y-axis dipoles, the factor $\vec{p}_{\eta,i}(t) \cdot \hat{R}_\eta$ from Eq. (10) is small for fluctuators close to the line connecting the two quantum dots. $\vec{p}_{\eta,i}(t) \cdot \hat{R}_\eta = 0$ for y-axis dipoles along this line. From this, we would expect the correlation strength to be smallest for y-axis dipoles, and this is seen in Fig. 6(a). As seen in Fig. 6(b), the dipole potentials at quantum dots 1 and 2 for x-axis dipoles are π radians out of phase. Since the quantum dots lie along the x-axis, any fluctu-

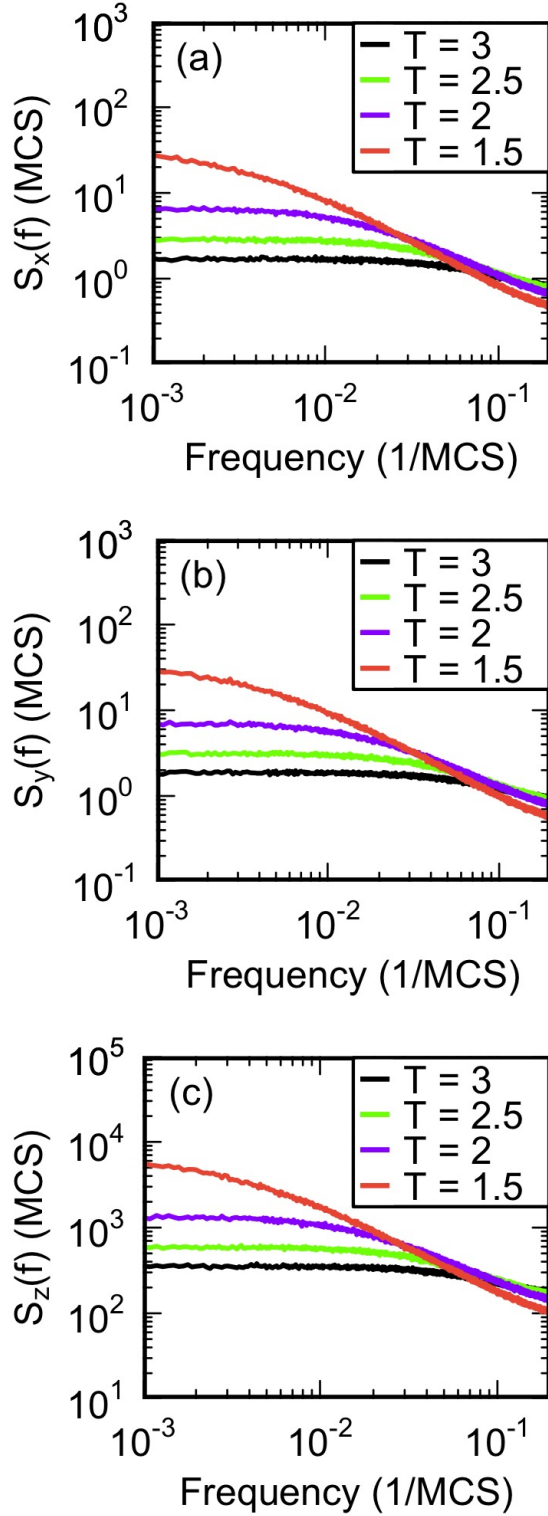


FIG. 10. Log-log plots of the electric potential noise power versus frequency at QD 1 for fluctuating dipoles that lie along the (a) x-axis, (b) y-axis, and (c) z-axis. All plots are the result of averaging over 200 runs with a QD separation of 10 lattice spacings.

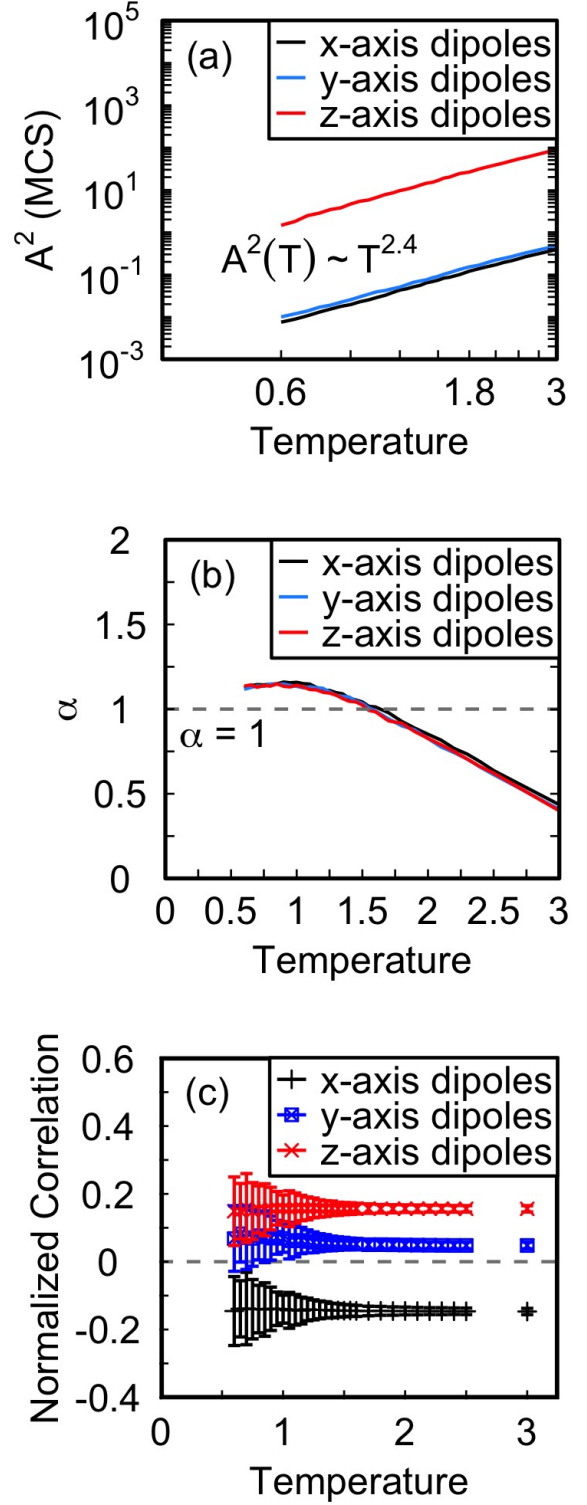


FIG. 11. (a) Log-log plot of temperature dependence of the noise amplitude, $A^2(T)$, obtained from fits to the noise power. (b) Plot of the temperature dependence of the noise exponent, $\alpha(T)$, obtained from fits to the noise power. (c) Plots of noise correlation between QDs 1 and 2 vs. temperature calculated using Eq. (16). Plots (a)-(c) show results for dipoles lying along the x, y, and z axes. All plots are the result of averaging over 200 runs with QD separation of 10 lattice spacings.

ations in x-axis dipoles between the quantum dots will have the opposite effect on each dot.

The image dipoles are aligned for the component along the z-axis and antialigned for the components along the x and y axes (see Fig. 3), so we expect the dipole potential calculated from the z-axis component to be the most significant. For the electric dipoles with random orientations, the results should be similar to the case of dipoles aligned along the z-axis. This is certainly true for the dipole correlations and the noise exponents. However, the noise power and noise amplitudes resulting from electric dipoles aligned along the z-axis are three times larger. This is expected, since the z-axis dipoles have unit length, but the z components of the randomly-oriented dipoles have a typical length of $1/\sqrt{3}$. This corresponds to a factor of $1/\sqrt{3}^2 = 1/3$ that reduces the noise amplitude.

- [1] J. Yoneda, K. Takeda, T. Otsuka, T. Nakajima, M. R. Delbecq, G. Allison, T. Honda, T. Kodera, S. Oda, Y. Hoshi, N. Usami, K. M. Itoh, and S. Tarucha, A quantum-dot spin qubit with coherence limited by charge noise and fidelity higher than 99.9%, *Nature Nanotechnology* **13**, 102 (2018).
- [2] E. J. Connors, J. Nelson, and J. M. Nichol, Charge-noise spectroscopy of Si/SiGe quantum dots via dynamically-decoupled exchange oscillations, *Nature Communications* **13**, 940 (2022).
- [3] P. Dutta, P. Dimon, and P. M. Horn, Energy scales for noise processes in metals, *Phys. Rev. Lett.* **43**, 646 (1979).
- [4] P. Dutta and P. M. Horn, Low-frequency fluctuations in solids: $\frac{1}{f}$ noise, *Rev. Mod. Phys.* **53**, 497 (1981).
- [5] L. Petit, H. G. J. Eenink, M. Russ, W. I. L. Lawrie, N. W. Hendrickx, S. G. J. Philips, J. S. Clarke, L. M. K. Vandersypen, and M. Veldhorst, Universal quantum logic in hot silicon qubits, *Nature* **580**, 355 (2020).
- [6] E. J. Connors, J. Nelson, H. Qiao, L. F. Edge, and J. M. Nichol, Low-frequency charge noise in Si/SiGe quantum dots, *Phys. Rev. B* **100**, 165305 (2019).
- [7] E. J. Connors, J. Nelson, H. Qiao, L. F. Edge, and J. M. Nichol, Erratum: Low-frequency charge noise in Si/SiGe quantum dots [*Phys. Rev. B* 100, 165305 (2019)], *Phys. Rev. B* **102**, 039902(E) (2020).
- [8] L. Petit, J. M. Boter, H. G. J. Eenink, G. Droulers, M. L. V. Tagliaferri, R. Li, D. P. Franke, K. J. Singh, J. S. Clarke, R. N. Schouten, V. V. Dobrovitski, L. M. K. Vandersypen, and M. Veldhorst, Spin lifetime and charge noise in hot silicon quantum dot qubits, *Phys. Rev. Lett.* **121**, 076801 (2018).
- [9] S. Ahn, S. Das Sarma, and J. P. Kestner, Microscopic bath effects on noise spectra in semiconductor quantum dot qubits, *Phys. Rev. B* **103**, L041304 (2021).
- [10] R. E. Throckmorton and S. D. Sarma, A generalized model of the noise spectrum of a two-level fluctuator in the presence of an electron subbath (2023), arXiv:2305.14348 [cond-mat.mes-hall].
- [11] D. Mickelsen, H. M. Carruzzo, S. N. Coppersmith, and C. C. Yu, Effects of temperature fluctuations on charge noise in quantum dot qubits (2023), arXiv:1234.56789.
- [12] J. Yoneda, J. S. Rojas-Arias, P. Stano, K. Takeda, A. Noiri, T. Nakajima, D. Loss, and S. Tarucha, Noise-correlation spectrum for a pair of spin qubits in silicon (2022).
- [13] J. S. Rojas-Arias, A. Noiri, P. Stano, T. Nakajima, J. Yoneda, K. Takeda, T. Kobayashi, A. Sammak, G. Scappucci, D. Loss, and S. Tarucha, Spatial noise correlations beyond nearest-neighbor in $^{28}\text{Si}/\text{SiGe}$ spin qubits (2023), arXiv:2302.11717 [cond-mat.mes-hall].
- [14] X. Hu and S. Das Sarma, Charge-fluctuation-induced dephasing of exchange-coupled spin qubits, *Phys. Rev. Lett.* **96**, 100501 (2006).
- [15] D. Culcer, X. Hu, and S. Das Sarma, Dephasing of Si spin qubits due to charge noise, *Applied Physics Letters* **95**, 073102 (2009), <https://pubs.aip.org/aip/apl/article-pdf/doi/10.1063/1.3194778/14105785/073102.1.online.pdf>.
- [16] G. Ramon and X. Hu, Decoherence of spin qubits due to a nearby charge fluctuator in gate-defined double dots, *Phys. Rev. B* **81**, 045304 (2010).
- [17] Q. Li, L. Cywiński, D. Culcer, X. Hu, and S. Das Sarma, Exchange coupling in silicon quantum dots: Theoretical considerations for quantum computation, *Phys. Rev. B* **81**, 085313 (2010).
- [18] D. Culcer and N. M. Zimmerman, Dephasing of Si singlet-triplet qubits due to charge and spin defects, *Applied Physics Letters* **102**, 232108 (2013), <https://pubs.aip.org/aip/apl/article-pdf/doi/10.1063/1.4810911/14275997/232108.1.online.pdf>.
- [19] P. Huang, N. M. Zimmerman, and G. W. Bryant, Spin decoherence in a two-qubit cphase gate: the critical role of tunneling noise, *npj Quantum Inf.* **4**, 62 (2018).
- [20] X.-C. Yang and X. Wang, Suppression of charge noise using barrier control of a singlet-triplet qubit, *Phys. Rev. A* **96**, 012318 (2017).
- [21] Y.-P. Shim and C. Tahan, Barrier versus tilt exchange gate operations in spin-based quantum computing, *Phys. Rev. B* **97**, 155402 (2018).
- [22] U. Güngördü and J. P. Kestner, Indications of a soft cut-off frequency in the charge noise of a Si/SiGe quantum dot spin qubit, *Phys. Rev. B* **99**, 081301 (2019).
- [23] F. Beaudoin and W. A. Coish, Microscopic models for charge-noise-induced dephasing of solid-state qubits, *Phys. Rev. B* **91**, 165432 (2015).
- [24] C. King, J. S. Schoenfeld, M. J. Calderón, B. Koiller, A. Saraiva, X. Hu, H. W. Jiang, M. Friesen, and S. N. Coppersmith, Lifting of spin blockade by charged impurities in Si-MOS double quantum dot devices, *Phys. Rev. B* **101**, 155411 (2020).
- [25] C. C. Yu, Possible mechanism for thermal conductivity in $(\text{KBr})_{1-x}(\text{KCN})_x$, *Phys. Rev. B* **32**, 4220 (1985).
- [26] A. G. Fowler, M. Mariantoni, J. M. Martinis, and A. N. Cleland, Surface codes: Towards practical large-scale quantum computation, *Phys. Rev. A* **86**, 032324 (2012).
- [27] S. Hunklinger and A. K. Raychaudhuri, Thermal and elastic anomalies in glasses at low temperatures, *Prog. in Low Temp. Phys.* **9**, 265 (1986).
- [28] W. A. Phillips, Two-level states in glasses, *Rep. Prog. Phys.* **50**, 1657 (1987).
- [29] P. W. Anderson, B. I. Halperin, and C. M. Varma, Anomalous low-temperature thermal properties of glasses and spin glasses, *The Philosophical Magazine: A Journal of Theoretical Experimental and Applied Physics* **25**, 1 (1972), <https://doi.org/10.1080/14786437208229210>.
- [30] W. A. Phillips, Tunneling states in amorphous solids, *Journal of Low Temperature Physics* **7**, 351 (1972).
- [31] C. C. Yu and A. J. Leggett, Low temperature properties of amorphous materials: Through a glass darkly, *Comments Cond. Mat. Phys.* **14**, 231 (1988).
- [32] D. J. Salvino, S. Rogge, B. Tigner, and D. D. Osheroff, Low temperature AC dielectric response of glasses to high DC electric fields, *Phys. Rev. Lett.* **73**, 268 (1994).
- [33] H. M. Carruzzo, E. R. Grannan, and C. C. Yu, Nonequilibrium dielectric behavior in glasses at low temperatures: evidence for interacting defects, *Phys. Rev. B* **50**, 6685 (1994).
- [34] J. Joffrin and A. Levelut, Virtual phonon exchange in glasses, *J. Phys. France* **36** (1975).
- [35] H. M. Carruzzo and C. C. Yu, Why phonon scattering in glasses is universally small at low temperatures, *Phys.*

- Rev. Lett. **124**, 075902 (2020).
- [36] S. Kogan, *Electronic Noise and Fluctuations in Solids* (Cambridge University Press, Cambridge, 1996).
- [37] L. Faoro and L. B. Ioffe, Quantum two level systems and kondo-like traps as possible sources of decoherence in superconducting qubits, Phys. Rev. Lett. **96**, 047001 (2006).
- [38] M. Constantin, C. C. Yu, and J. M. Martinis, Saturation of two-level systems and charge noise in josephson junction qubits, Phys. Rev. B **79**, 094520 (2009).
- [39] N. Metropolis, A. W. Rosenbluth, M. N. Rosenbluth, A. H. Teller, and E. Teller, Equation of state calculations by fast computing machines, J. Chem. Phys. **21**, 1087 (1953).
- [40] R. N. Bhatt and A. P. Young, Numerical studies of ising spin glasses in two, three, and four dimensions, Phys. Rev. B **37**, 5606 (1988).
- [41] W. H. Press, S. A. Teukolsky, W. T. Vetterling, and B. P. Flannery, *Numerical Recipes in C: The Art of Scientific Computing* (Cambridge University Press, New York, 1992).
- [42] M. Frigo and S. G. Johnson, The design and implementation of FFTW3, Proceedings of the IEEE **93**, 216 (2005), special issue on “Program Generation, Optimization, and Platform Adaptation”.
- [43] R. M. Jock, N. T. Jacobson, M. Rudolph, D. R. Ward, M. S. Carroll, and D. R. Luhman, A silicon singlet-triplet qubit driven by spin-valley coupling, Nature Comm. **13**, 641 (2022).
- [44] C. C. Yu and H. M. Carruzzo, Frequency dependence and equilibration of the specific heat of glass-forming liquids, Phys. Rev. E **69**, 051201 (2004).